DE GRUYTER Green Processing and Synthesis 2023; 12: 20230066

Research Article

Yanhong Cui, Yanhua Suo, Wei Zhang, Yingjun Wang*, Chunhong Nie, and Yanhong Wang

Preparation of Pd/Ce(F)-MCM-48 catalysts and their catalytic performance of *n*-heptane isomerization

https://doi.org/10.1515/gps-2023-0066
received April 17, 2023; accepted July 24, 2023

Abstract: Ce and F were added to MCM-48 molecular sieve by hydrothermal synthesis, and Pd/Ce(F)-MCM-48 metal acid bifunctional catalysts were prepared by impregnation method. The physical and chemical properties of Ce(F)-MCM-48 and Pd/Ce(F)-MCM-48 were characterized by X-ray diffraction, scanning electron microscope, NH_3 temperature programmed desorption instrument, Fourier infrared spectrometer, and X-ray photoelectronic spectrometer characterization methods. The results showed that when the molar ratio of the raw materials was n(Ce):n(TEOS) = 0.02 and n(NaF):n(TEOS) = 0.10, Ce(F)-MCM-48-0.10 molecular sieve had a high degree of order and large specific surface area and pore volume, the total acid content increased, and the acid strength also increased. And it had an acidic center and generated certain oxygen vacancies. The catalyst prepared after Pd impregnation had good dispersibility. 0.4% Pd/Ce(F)-MCM-48-0.10 catalyst still maintained the crystalline phase of MCM-48 molecular sieve. A micro-reaction device was used to examine the catalytic performance of *n*-heptane isomerization of Pd/Ce(F)-MCM-48-0.10 catalysts. When the hydrogen flow rate was $30\,\text{mL·min}^{-1}$, reduction temperature was 300°C, reduction time was 4 h, weight hourly space velocity was $7.6\,\text{h}^{-1}$, and reaction temperature was 280°C, 0.4% Pd/Ce(F)-MCM-48-0.10 catalyst was used in the heptane isomerization reaction, where the conversion of *n*-heptane was 67.3% and the selectivity of isoheptane was 96.5%.

Keywords: Pd/Ce (F)-MCM-48 catalyst, fluorine, cerium, *n*-heptane, isomerization

1 Introduction

With the promulgation of the EU's Euro V and Euro VI vehicle emission standards and the enhanced global awareness of energy conservation, emission reduction, and environmental protection [1], relevant environmental protection regulations had become stricter in terms of pollutant types and limits. To adapt to stricter emission regulations while meeting the demands of engine technology, the problems relating to pollutant emissions reduction, gasoline quality improvement, and the presence of *n*-alkane with zero octanes in straight-run gasoline must be resolved. Since straight-run gasoline contained multiple *n*-paraffins, the best way to improve the octane number was to convert straight chain alkanes into branched chain alkanes. Consequently, n-alkane isomerization had become an important process in the refining industry [2–4]. Some recognized industrialized technologies [5] had been developed for the isomerization of relatively short straight-chain (C_5 and C_6) alkanes, but satisfactory mature technologies for the isomerization of long straight-chain ($\geq C_7$) alkanes were still not available [6]. Accordingly, the development of catalysts for *n*-heptane isomerization had become an important issue.

Many materials can serve as a promising candidate for catalyst supports to immobilize the active species [7], Xie et al. [8,9] prepared a core–shell structured Fe_3O_4-MCM-41 nanocomposite, and the lipase and sodium silicate were successfully immobilized on the core–shell structured support, respectively. It was shown that the immobilized lipase and sodium silicate had good catalytic activity for transesterification of lard and soybean oil. Most catalysts used in *n*-heptane isomerization reactions were metal/support bifunctional

---

*** Corresponding author: Yingjun Wang,** College of Chemistry and Chemical Engineering, Northeast Petroleum University, Daqing 163318, China, e-mail: wangying-jun@163.com
Yanhong Cui: College of Chemistry and Chemical Engineering, Northeast Petroleum University, Daqing 163318, China; National Coarse Cereals Engineering Research Center, Heilongjiang Bayi Agricultural University/Quality Supervision, Inspection and Test Center of Agricultural and Processed Products (Daqing), Ministry of Agriculture and Rural Affairs, Daqing 163319, China
Yanhua Suo, Wei Zhang, Chunhong Nie: College of Chemistry and Chemical Engineering, Northeast Petroleum University, Daqing 163318, China
Yanhong Wang: College of Horticultural, Science Heilongjiang Bayi Agricultural University, Daqing 163319, China

catalysts. The structural characteristics and acidic properties of these catalyst supports had a considerable influence on the isomerization of straight-chain heptane. Regarding the preparation of support materials, MCM-48 was considered important. For the pure silicon MCM-48 molecular sieve, the surface of the silicon-oxygen tetrahedron was a charge balance system with a low acid concentration due to fewer lattice defects in its skeleton. As a result, there was a lack of catalytic active sites which limited the application and required some functional modifications to the mesoporous molecular sieve. Currently, the method of introducing heteroatoms is widely used [10]. Scholars had successively replaced some elements with similar properties, such as Fe and Co [11], and Mo and Al [12,13], with skeleton silicon elements, forming special metal complex heteroatomic molecular sieves. Another important support modification strategy was to introduce anions such as F^-, Cl^-, S^{2-}, N^{3-}, etc., [14] into the molecular sieve skeleton. Among them, fluorine possessed unique properties such as high electronegativity and a small atomic radius [15]. Recently, Jiang et al. [16] synthesized a fluorine-enhanced Pd/HZSM-5 catalyst whose surface morphology, hydrophobicity, acidity, and electronic properties could be regulated by the doping amount of fluorine, and the catalyst demonstrated good catalytic activity for the hydrodeoxygenation of acetophenone. Yang et al. [17] prepared an anionic fluorine-doped $La_{0.6}Sr_{0.4}Fe_{0.8}Ni_{0.2}O_{3-\delta}$ perovskite cathode material with enhanced electrocatalytic activity. Some progress had been made in several catalytic material studies, where their surface and structure had been modified to attain special physical and chemical properties.

The nano-sized porous materials, as used for the preparation of solid catalysts, can permit the higher loading of active species and better access of the active sites [18,19]. Roy et al. [20] synthesized the novel mesoporous catalysts consisting of Ru and Fe_3O_4 nanoparticles (NPs) impregnated over ceria promoted 2D-hexagonal SBA-15 type mesoporous silica material and employed it in the CO_2 reduction reaction. Optimal process conditions could render much higher CO_2 conversion efficacy for selective methane synthesis in comparison with previous investigations. However, studies regarding the catalytic performance of *n*-heptane isomerization with a Pd-loaded catalyst on MCM-48 molecular sieves modified by Ce and F simultaneously had not been reported yet.

The novelty of this study was that Ce(F)-MCM-48 molecular sieve was prepared by hydrothermal synthesis, while Pd/Ce(F)-MCM-48 bimetallic catalyst was prepared by impregnation method. Pd NPs were used as catalytic active sites [21], Ce was used as catalyst additives to mainly increase the acidity of molecular sieve support, Ce-MCM-48 provided alkane isomerization sites [3], F doping took away part of oxygen to produce surface defects and oxygen vacancies, which was conducive to anchoring metal Pd atoms [22], making Pd NPs have good dispersion. Based on the characterization results, the effects of Ce and F introduction on the structure of the support and catalyst were discussed, and then the catalytic performance of these catalysts in *n*-heptane isomerization was investigated on a microreactor. It was hoped that such catalysts would be applied in the development of long-chain alkane isomerization catalysts, thereby laying a theoretical foundation for the production of green and clean gasoline.

2 Materials and methods

2.1 Materials

Tetraethyl orthosilicate (TEOS, AR), sodium fluoride (NaF, AR) were purchased from Tianjin Damao Chemical Reagent Factory, cetyltrimethylammonium bromide (CTAB, AR), cerous nitrate [$Ce(NO_3)_3 \cdot 6H_2O$] and palladium nitrate [$Pd(NO_3)_2 \cdot 2H_2O$, AR] were purchased from Sinopharm Chemical Reagent Co. Ltd, sodium hydroxide (NaOH, GR) was purchased from Tianjin Kemiou Chemical Reagent Co. Ltd, absolute ethyl alcohol (AR) was purchased from Liaoning Quanrui Reagent Co. Ltd, *n*-heptane (AR) was purchased from Shenyang East China Reagent Factory, deionized water from a Milli-Q System was used in all experiments, and hydrogen (volume fraction 99.99%) was purchased from Daqing Xuelong Gas Station.

2.2 Synthesis of the Ce(F)-MCM-48 mesoporous material

Under alkaline conditions, CTAB was used as the template, and $Ce(NO_3)_3 \cdot 6H_2O$ and NaF were used as the added reagents, Ce(F)-MCM-48 was synthesized by hydrothermal method.

First, NaOH was dissolved in deionized water. Then, $Ce(NO_3) \cdot 6H_2O$ and NaF were stirred at 35°C for 0.5 h and CTAB was gradually added to the above solution and stirred for 1.5 h until the mixtures became clear and transparent, and then TEOS was added dropwise to the mixture by pipette and stirred for 1 h. The molar ratio of reactant raw materials was $n(\mathrm{TEOS}):n(\mathrm{CTAB}):n(H_2O):n(\mathrm{NaOH}):n(\mathrm{Ce}):n(\mathrm{NaF})$ = 1.0:0.65:62:0.5:0.02:x (x = 0, 0.05, 0.10, 0.15). The initial as-prepared gel was transferred into a stainless-steel reactor lined with polytetrafluoroethylene and placed in a drying oven for crystallization at 120°C for 72 h. The product was washed and filtered with water and dried at 90°C for 6 h on a polytetrafluoroethylene-coated electric heating plate, further dried at 105°C for 5 h in an electric blast drying oven, and calcinated at 550°C for 6 h in a box-type resistance furnace.

The prepared sample was marked as Ce(F)-MCM-48-*x*, and when $x = 0$, it was marked as Ce-MCM-48. MCM-48 was synthesized without the addition of $Ce(NO_3)_3 \cdot 6H_2O$ and NaF, which was marked as MCM-48, and the other steps were the same as above.

2.3 Preparation of Pd/Ce(F)-MCM-48 catalyst

Pd-loaded catalysts with mass fractions of 0.4% were prepared by impregnation method. $Pd(NO_3)_2 \cdot 2H_2O$ was dissolved in deionized water, Ce(F)-MCM-48-0.10 was then immersed in the solution which was then subjected to ultrasonic dispersion at 50°C for 0.5 h. Subsequently, the solution was left in a static state at room temperature overnight, the drying steps were same as 2.2. Then, the above mixtures were calcinated at 400°C for 4 h in a resistance furnace, 0.4% Pd/Ce(F)-MCM-48-0.10 catalysts were obtained. Pd/MCM-48 and Pd/Ce-MCM-48 catalysts were prepared using the same method.

2.4 Characterization of catalysts

An X-ray diffractometer (XRD, smartLAB SE, Japanese Rigaku Corporation) was used for crystal structure analysis with Cu Kα as the radiation source operated at the tube voltage of 40 kV and tube current of 40 mA. A scanning electron microscope (SEM, Hitachi High-Technologies S-4800II, Japan) was used for the microscopic surface morphology analysis of the molecular sieve samples. A Fourier infrared spectrometer (FT-IR, AVATAR-360, American Thermo Nicolet) was used for infrared spectroscopy analysis of the samples. A specific surface area and pore size test analyzer (TriStar II, American Micromeritics) was used to determine the structural parameters of the sample. An ion chromatograph (SGB-YY101040H, American Thermo Fisher) was used to characterize the F content. An inductively coupled plasma optical emission spectrometer (ICP-OES, Optima8000, American PerkinElmer) was used to characterize the Pd and Ce content. An NH_3 temperature programmed desorption instrument (NH_3-TPD, Autochem II 2920, American Micromeritics) was used to test the surface acid content and acid intensity distribution of the samples. A transmission electron microscope (TEM, JEM-2100PLUS, Japanese JEOL Ltd) was used to record the sample images with an acceleration voltage of 100–120 kV. A field emission scanning electron microscope (FESEM, Czech TESCAN MIRA LMS) with energy dispersive spectroscopy (EDS) was used for the surface morphology evaluation. An X-ray photoelectronic spectrometer (XPS, American Thermo Fisher Nexsa type) was used for the qualitative and quantitative characterization of the chemical state of the surface elements of the samples. An infrared spectrometer (VERTEX 70, German Bruker) was used for the pyridine infrared spectroscopy analysis of the samples. A gas chromatograph (GC-7980A, Zhengzhou, China) was used to analyze the heptane isomer products.

2.5 Evaluation of the *n*-heptane hydroisomerization reaction

The catalytic reaction performance experiment was conducted in a micro fixed-bed reactor under atmospheric pressure. The catalyst powder was pressed and sieved to collect 60–80 mesh particles for use. Then, 0.40 g particles were placed in the reaction tube (inner diameter 6 mm). The catalyst was activated in a hydrogen atmosphere for 4 h at 400°C before the reaction, and then the temperature was lowered to the required reaction temperature. The reaction evaluation was performed under the conditions of an H_2 flow rate of 30 $mL \cdot min^{-1}$, molar ratio of $n(H_2):n(C_7H_{16}) = 12$, and WHSV of 7.6 h^{-1}. After the reaction was stable for 0.5 h, the sample was taken, and the product was analyzed online by gas chromatograph FID detector. The catalytic performance was evaluated via the conversion rate (*x*) of *n*-heptane, the selectivity (*s*), and the yield (*y*) of the product. These can be calculated by Eqs. 1–3 as follows:

$$x(\%) = \frac{\text{The amount of } n\text{-heptane consumed in the reaction}}{\text{The amount of } n\text{-heptane passed in the reaction}} \times 100\% \tag{1}$$

$$s(\%) = \frac{\text{The amount of isoheptane generated in the reaction}}{\text{The amount of } n\text{-heptane consumed in the reaction}} \times 100\% \tag{2}$$

$$y(\%) = \frac{\text{The amount of isoheptane generated in the reaction}}{\text{The amount of } n\text{-heptane passed in the reaction}} \times 100\% \tag{3}$$

3 Results and discussion

3.1 Effect of NaF doping on the preparation of the support.

Figure 1 showed the small-angle XRD of Ce(F)-MCM-48-*x* mesoporous material. All the five materials showed strong (211) diffraction peaks at $2\theta = 2$–$3°$ [23]. Compared with MCM-48, the intensity of the (211) diffraction peak of Ce-MCM-48 decreased and the (220) diffraction peak almost disappeared, the phenomenon of peak broadening appeared. This indicated that the crystallinity decreased after the doping of Ce. When *n*(F):*n*(Si) was 0.05, the (211) diffraction peak was enhanced and the (220) diffraction peak was clearly visible. When *n*(F):*n*(Si) was 0.10, the (420) and (332) diffraction peaks appeared and all the diffraction peaks became sharp, and the intensity was obviously enhanced. The resolution of the peak was better. Diffraction peaks at $2\theta = 4$–$5°$ all conformed to the I*a*3*d* (211, 220, 420, 332) space group of the characteristic MCM-48 diffraction peaks [13]. This was the main factor that contributed to the good chemical stability of the material molecules. The hydration layer of CTAB and silicate can be effectively removed by adding F-anions with strong self-hydration tendency in the synthesis system. The key condition for the synthesis of cubic MCM-48 was to facilitate the formation and growth of CTAB micelles and increase the g value [24]. According to literature report [25], F^- and O^{2-} had equivalent ionic radius, and the addition of F^- would replace part of O^{2-}, which would destroy the lattice structure of some oxides. The oxide crystal was distorted, and unsaturated bonds were generated on its surface, which could increase the lattice defects of oxides. When *n*(F):*n*(Si) was 0.15, the intensity of each diffraction peak decreased, the possible reason was that the excessive doping of F^{-1} in the system led to the continuous destruction of the oxide lattice, causing local pore collapse and the decrease in the order of pore structure. Therefore, the optimal concentration of *n*(F):*n*(Si) was 0.10. At this ratio, F and Ce synergistically promoted the polymerization of silicates, resulting in better crystallization. In subsequent experiments, the Ce(F)-MCM-48-0.10 was selected as the support for F-doping.

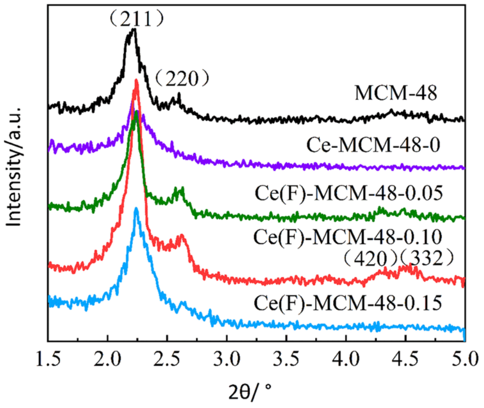

Figure 1: XRD patterns of MCM-48 and Ce(F)/MCM-48-*x* (*x* = 0, 0.05, 0.10, 0.15).

Figure 2 displayed the SEM images of MCM-48, Ce-MCM-48, and Ce(F)-MCM-48-0.10. The MCM-48 mesoporous material synthesized by conventional hydrothermal synthesis had a spherical particle morphology accompanied by a small amount of agglomeration and small particles with good regularity and purity [11]. After Ce was doped, the morphology became irregular, accompanied by pits, broken hemispheres, and agglomeration. For mesoporous material synthesized with the addition of F, recombination occurred in the crystal cage due to further changes in the chemical bonds, where the silicate was re-polymerized to form regular spherical particles of uniform size [26]. The order and purity were greatly improved and more spheres with a particle size of nearly 1 μm were generated. This indicated that the introduction of F was conducive to the formation of a cubic phase of MCM-48 structure.

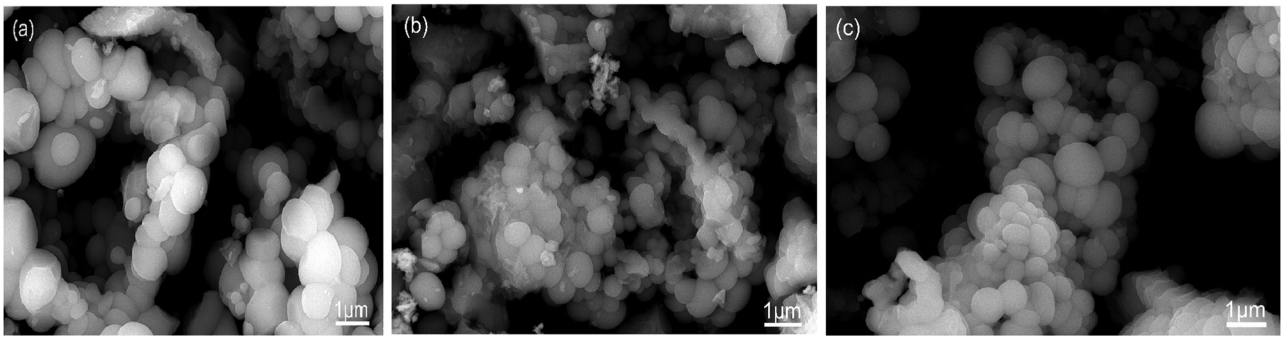

Figure 2: SEM images of the products of (a) MCM-48, (b) Ce-MCM-48, and (c) Ce(F)-MCM-48-0.10.

Furthermore, the introduction of Ce and F weakened the force between inorganic and organic interfaces. Under the action of surfactants, SiO_2 was arranged in an orderly manner according to certain crystallographic rules to obtain a crystalline mesoporous material [14]. This series of changes was consistent with the XRD pattern of the samples in Figure 1.

3.2 N_2 adsorption–desorption and texture properties

Figure 3a shows the N_2 adsorption–desorption isotherms of MCM-48, Ce-MCM-48, Ce(F)-MCM-48-0.10, 0.4% Pd/Ce-MCM-48, and 0.4% Pd/Ce(F)-MCM-48-0.10 which can all be classified as Langmuir IV isotherms and exhibited H_4 hysteresis loops. The hysteresis loop of the samples showed an obvious change within the range of relative pressure p/p_0 of about 0.4–0.9, indicating the presence of large mesopores produced by inter-particle space [27]. Figure 3b shows the pore size distribution curve. The pore size distribution was obtained by the Barrett–Joyner–Halenda equation. The Ce-MCM-48 pore size distribution range was slightly larger than that of MCM-48, while that of Ce(F)-MCM-48-0.10 narrowed with the trend of the H4 hysteresis loop, which confirmed the existence of uniform and cylindrical mesopores [28].

Based on Figure 3b and Table 1, it can be seen that due to the Ce ions in Ce-MCM-48 having a larger radius than the Si ions, the length of the Ce–O bond was longer than that of the Si–O bond [29], causing the stretching of the skeleton and the increase in average pore size. Further increase in the surface area and total pore volume of Ce(F)-MCM-48-0.10 did not cause any spatial steric resistance of the pore channels on the skeleton. The Ce(F)-MCM-48-0.10 pore size was also further enlarged, and the mesopore size tended to be uniform. The synergy of F and Ce enabled the support frame to form a new structure [26], which was also consistent with the XRD pattern in Figure 1.

As shown in Table 1, the actual loading content of Ce in Ce(F)-MCM-48-0.10 was slightly reduced, and the doping of F did not cause serious Ce peeling with the actual loading percentage of 53.3% and 65.5%, respectively. According to ion chromatography test, the mass fraction of F in Ce (F)-MCM-48-0.10 was 1.51%. F and Ce can be loaded on the skeleton simultaneously. Due to the Ce(F)-MCM-48-0.10, specific surface area and pore volume were the largest, the adsorption performance of the molecular sieves improved. Both the specific surface area and pore volume of the 0.4% Pd/Ce(F)-MCM-48-0.10 catalyst were reduced slightly,

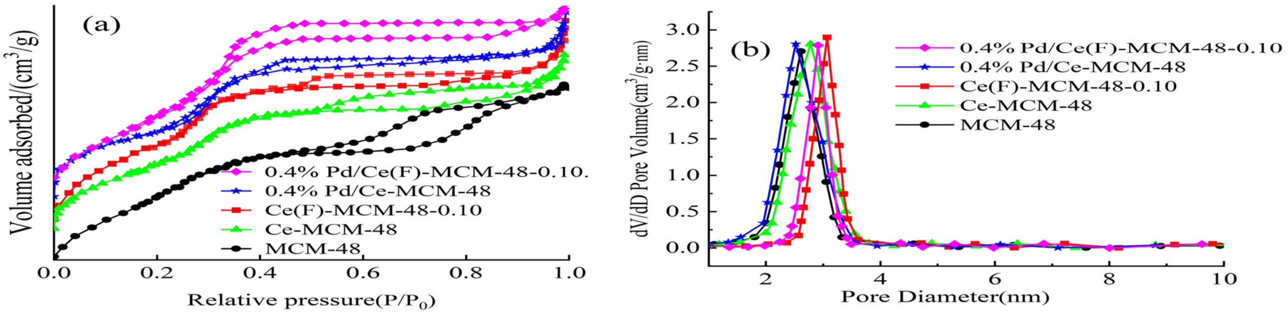

Figure 3: N_2 adsorption–desorption isotherms (a) and pore size distributions (b) of MCM-48, Ce-MCM-48, Ce(F)-MCM-48-0.10, 0.4% Pd/Ce-MCM-48, and 0.4% Pd/Ce(F)-MCM-48-0.10.

Table 1: Physical properties of the samples

Sample	Surface area ($m^2 \cdot g^{-1}$)	Pore volume ($cm^3 \cdot g^{-1}$)	Average pore diameter (nm)	Pd (loading rate, wt%)	Ce (loading rate, wt%)	F (loading rate, wt%)
MCM-48	897.1	0.93	2.61	—	—	—
Ce-MCM-48	972.6	0.97	2.78	—	66.5	—
Ce(F)-MCM-48-0.10	1,323.2	1.17	3.07	—	65.5	53.3
0.4% Pd/Ce-MCM-48	894.2	0.95	2.52	97.5	60.5	—
0.4% Pd/Ce(F)-MCM-48-0.10	1,293.0	1.13	2.91	97.8	65.0	52.9

indicating that Pd had been loaded on the support and that F had improved the structural performance. Benaissa et al. [30] reported four mesoporous supports loaded with palladiums, of which MCM-48 had the largest surface area. The effective load rate of Ce in 0.4% Pd/Ce-MCM-48 was 60.5%. While the effective load rate of Pd, F, and Ce were 97.8%, 52.9%, and 65.0%, respectively, and there was almost no loss of F and Ce after Pd impregnation. The ion chromatograph test results indicated that the mass fraction of F in 0.4% Pd/Ce(F)-MCM-48-0.10 was 1.45%.

3.3 Acidic properties

Figure 4 shows the NH_3-TPD of the support and catalysts. Each peak area corresponded to the acid strength of the acid center. Within the temperature range of 150–250°C, the NH_3 desorption peak corresponded to weak acid strength. Within the range of 250–400°C, the desorption peak corresponded to medium acid strength. There was no peak corresponding to the strong acid site. The order of acid content and strength of the acid sites of the samples was 0.4% Pd/Ce(F)-MCM-48-0.10 > 0.4% Pd/Ce-MCM-48 > Ce(F)-MCM-48-0.10 > Ce-MCM-48 > MCM-48 shown in Table 2. Catalysts with suitable weak acid and medium-strength acid would exhibit a high catalytic activity in isomerization reactions [31].

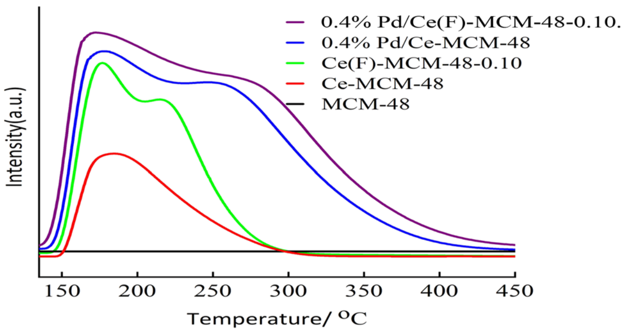

Figure 4: NH_3-TPD characterizations of different samples.

Table 2 shows the type and acid content of the acid center on the surface of the support and catalysts. The acid content of MCM-48 was negligible and the surface was nonacidic. After the Ce was doped, it formed a compound with the support. The Bronsted acid content increased due to the formation of Si–O–Ce bonds, the increase in Lewis acid content may be caused by the presence of CeO_2 in mesoporous materials [31]. The acid content also increased significantly after the introduction of F. This was because F had a similar radius to the hydroxyl groups and could exchange freely, allowing it to enter the skeleton to form a F–Si structure, releasing lattice oxygen. The function of fluoride was to provide L-acid centers [32,25]. The bridged hydroxyl group (SiF–OH) generated by the isomorphous replacement of the skeleton became the acidic center of the Ce(F)-MCM-48 support, which further increased the total number of acid content. For the Pd/Ce-MCM-48 catalyst, coordination bonds were generated following Pd impregnation, Pd provided Lewis acid, resulting in an increased content of acid sites and the total acid content.

3.4 Crystal structure

Figure 5a shows the small-angle XRD patterns of 0.4% Pd/MCM-48, 0.4% Pd/Ce-MCM-48, and 0.4% Pd/Ce(F)-MCM-48-0.10 catalyst materials prepared by the impregnation of the three supports in Pd. Compared with MCM-48 in Figure 1, the 0.4% Pd/Ce(F)-MCM-48 catalyst exhibited (211) and (220) strong diffraction peaks at 2θ = 2–3° while still exhibited typical MCM-48 characteristics, indicating a relationship with a high degree of support crystallization [13]. 0.4% Pd/MCM-48 and 0.4% Pd/Ce-MCM-48-0.10 only exhibited (211) diffraction peaks with a widened peak shape, but the (220) diffraction peak disappeared. Figure 5b shows the wide-angle XRD

Table 2: Acidity of MCM-48, Ce-MCM-48, Ce(F)-MCM-48-0.10, 0.4% Pd/Ce-MCM-48, and 0.4% Pd/Ce(F)-MCM-48-0.10

Sample	Brönsted acid ($mmol\cdot g^{-1}$)	Lewis acid ($mmol\cdot g^{-1}$)	Amount of acid site ($mmol\cdot g^{-1}$)	Amount of acid site ($mmol\cdot g^{-1}$)[a]
MCM-48	0.07	0.00	0.07	–
Ce-MCM-48	0.59	0.30	0.89	0.92
Ce(F)-MCM-48-0.10	0.72	0.52	1.24	1.43
0.4% Pd/Ce-MCM-48	1.45	2.93	4.38	2.76
0.4% Pd/Ce(F)-MCM-48-0.10	1.87	3.84	5.71	3.12

[a] The acid content is calculated from NH_3-TPD.

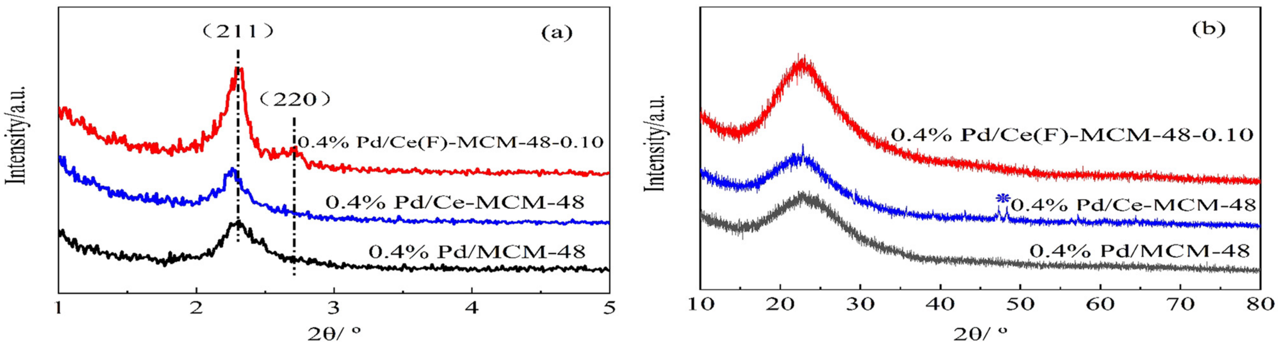

Figure 5: XRD patterns of Pd/MCM-48, Pd/Ce-MCM-48, and Pd/Ce(F)-MCM-48-0.10: (a) small-angle XRD and (b) wide-angle XRD.

patterns of the three corresponding materials, all of which had a wide peak at 2θ = 20–30°. There was a typical silicon-oxygen tetrahedron structure while the peak position remained unchanged. The signal strength of 0.4% Pd/Ce(F)-MCM-48-0.10 was enhanced, indicating that its degree of order was improved. 0.4% Pd/Ce-MCM-48 exhibited the (220) characteristic diffraction peak of CeO_2 cubic crystal at 2θ = 47.5° (JCPDS No. 34-0394) [33], but this peak was not observed in 0.4% Pd/Ce(F)-MCM-48-0.10, indicating that Ce was dispersed and assembled in the support skeleton after the introduction of F. No diffraction peaks of Pd species were observed in any of the three materials. This proved that the metal Pd can be well dispersed on the support surface. As shown in Figure 6, it was observed with TEM that the metal oxide clusters of 0.4% Pd/Ce-MCM-48 catalyst formed agglomerations, while the embedded Pd and Ce species were poorly dispersed. The 0.4% Pd/Ce(F)-MCM-48-0.10 catalyst did not exhibit a larger metal oxide crystal phase, indicating that it existed in the form of small particles, or formed metal oxide nanoparticles in the support pores [30]. The distinct hexagonal hole arrangement and different directions of crystal lattice stripes also reflected the three-dimensional direction and well-organized pore structure of the support.

3.5 Microscopic morphology and structure

Based on the SEM scanning and EDS spectroscopy analysis in Figure 7, the 0.4% Pd/Ce(F)-MCM-48-0.10 catalyst demonstrated a regular morphology with a smooth spherical surface. Pd and Ce oxide, as well as the particles of F, were evenly and successfully coated on MCM-48, without any signs of agglomeration or sintering. This can be attributed to the interaction between the chemical bonds formed on the support interface and the Pd particles, which drove the diffusion of Pd atoms to the cerium lattice. It could be inferred that Pd may be added to the cerium lattice in the MCM-48 space [34], which was consistent with the XRD results shown in Figure 5b. This indicated that Ce(F)-MCM-48-0.10 was a satisfactory support for dispersing Pd NPs.

3.6 Chemical environment

In Figure 8, the binding states of the elements in the samples were examined using the XPS spectrum. Figure 8a shows the full spectrum of the two samples. Figure 8b

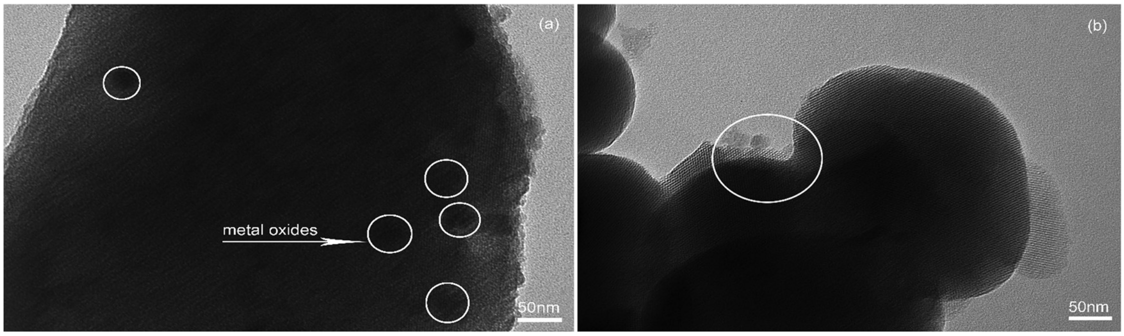

Figure 6: TEM image of (a) 0.4% Pd/Ce-MCM-48 and (b) 0.4% Pd/Ce(F)-MCM-48-0.10.

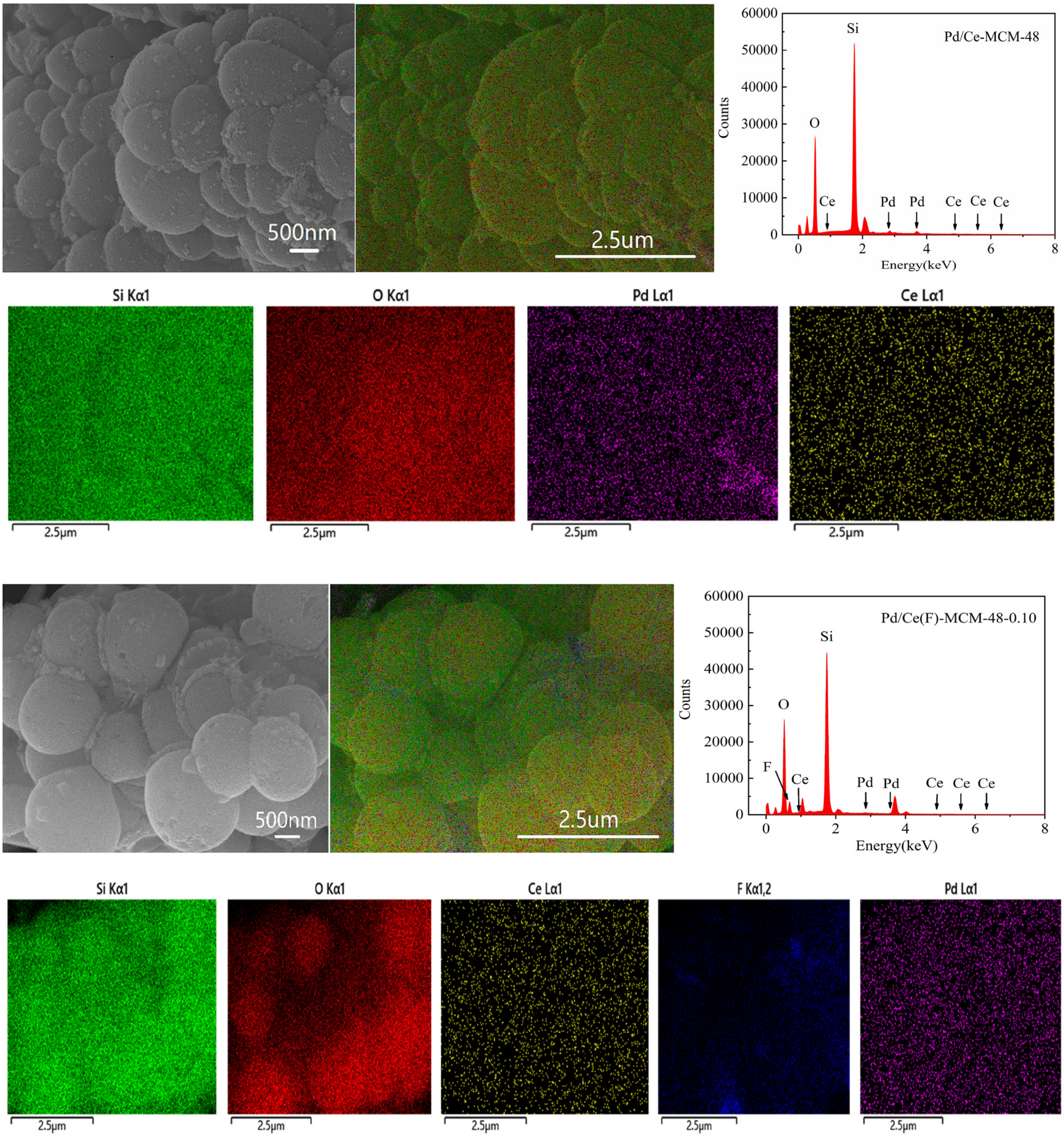

Figure 7: SEM images, EDX spectrum, and SEM mapping of Pd/Ce-MCM-48 and Pd/Ce(F)-MCM-48-0.10.

shows the fitted O1s spectra of the two samples. The O1s spectra can be deconvoluted to three peaks: lattice oxygen at 530.31 eV, oxygen modified by the nearby presence of an oxygen vacancy at 532.38 eV, and hydroxyl species at 533.3 eV [5,35–37]. This study had deviations, which was consistent with the literature reported, the hypothesis that the replacement of heavier atoms would cause the shift of the O1s peak towards the high binding energy side [38]. The oxygen vacancy areas in 0.4% Pd/Ce-MCM-48 and 0.4% Pd/Ce(F)-MCM-48-0.10 were measured to be 64.7%, and 72.5%, respectively. Oxygen vacancies would take away a pair of electrons [20], promoting metal Pd anchoring on the support [22]. Figure 8c shows the Si2p spectra. The deconvolution produced one peak at binding energies of 103.9 eV, which was assigned to Si^{4+} species, indicating that amorphous silica was the main phase of

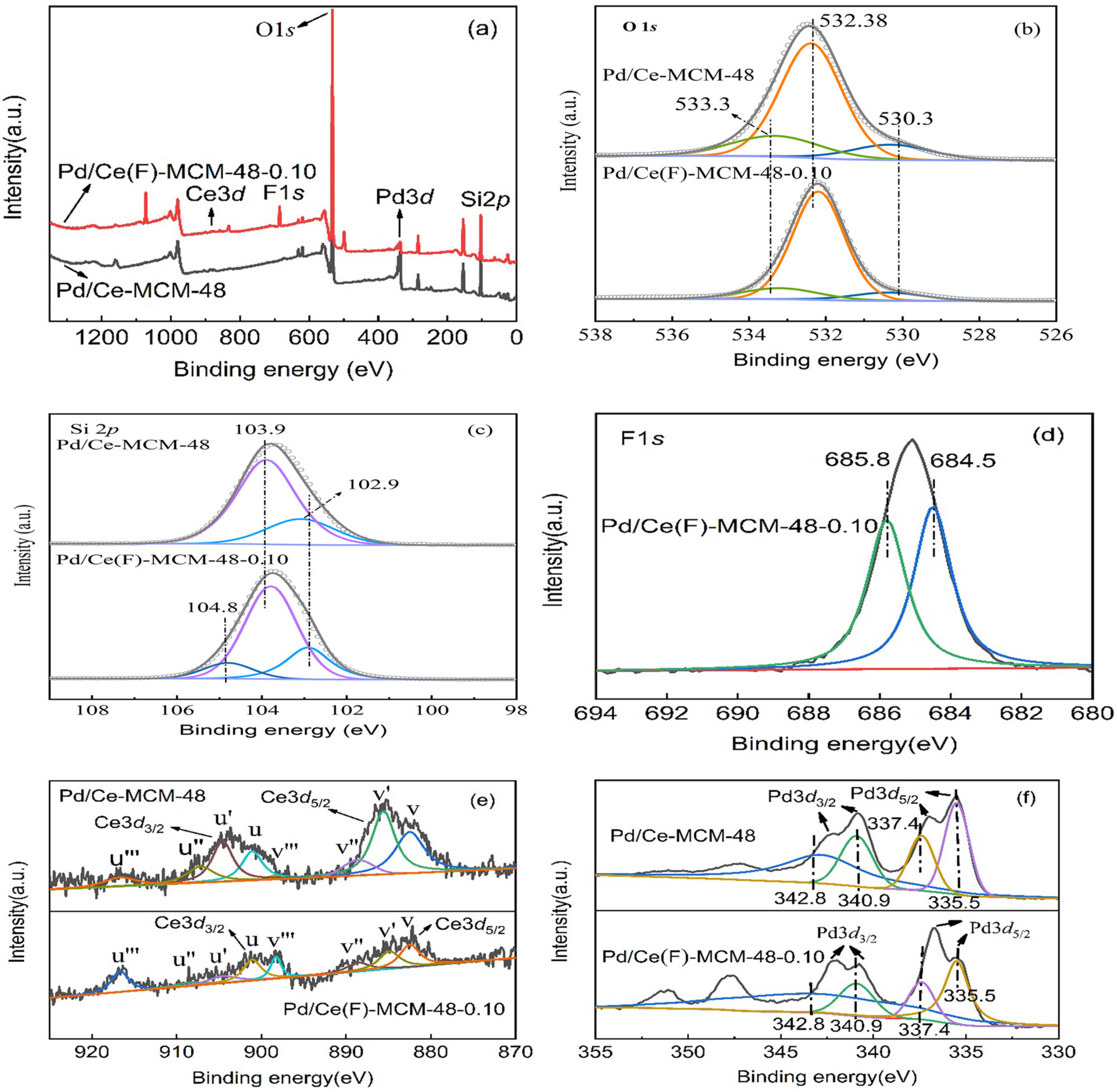

Figure 8: XPS spectra of Pd/Ce-MCM-48 and Pd/Ce(F)-MCM-48-0.10: (a) XPS full spectra, (b) O1s, (c) Si2p, (d) F1s, (e) Ce3d, and (f) Pd3d of Pd/Ce-MCM-48 and Pd/Ce(F)-MCM-48-0.10.

nanospheres. The peak near 102.9 eV was related to Si–O–Ce. It was worth noting that due to the strong electronegativity of F being higher than that of Si ion, the binding energy of F–Si was higher than that of Si–Si. The peak of 104.8 eV in 0.4% Pd/Ce (F)-MCM-48-0.10 was related to F–Si–O [39–41].

Figure 8d shows the F1s spectra. The characteristic peak at the binding energy of 684.5 eV was attributed to the covalent Si–F bond. F was at the binding energy of 685.8 eV, with high bonding energy [42,43,40]. Due to the hybridization of the Ce4f and ligand orbitals as well as the partial occupation of the 4f orbital, the Ce3d spectra in Figure 8(e) was relatively complex. There were two types of cerium oxide on the surface, namely, Ce^{3+} and Ce^{4+}. Ce^{3+} included V′ and u′, while Ce^{4+} included V, V″, V‴, u, u″, and u‴ [29,44]. As to the redox coupling Ce^{3+}/Ce^{4+}, it was generally believed that the presence of Ce^{3+} generated more surface defects and oxygen vacancies which helped improve the catalytic efficiency [45]. In the Pd3d spectra in Figure 8(f), the binding energy of Pd3d5/2 was 337.4 eV, which was attributable to the high dispersion of PdO [46]. The existence of Pd on the surface of the two supports was quite different, due to the different numbers and intensities of active sites on the surface of different supports. F modification can regulate the distribution of Pd3d core electrons and attract electrons from adjacent Pd to trigger charge transfer, thereby improving the stability of Pd particles in a higher oxidation state [16].

Figure 9 shows the FT-IR spectrum of the sample skeleton configuration for analysis. All three materials of Ce-MCM-48, Ce(F)-MCM-48-0.10, and Pd/Ce(F)-MCM-48-0.10 had skeleton vibration peaks at 810 and 1,088 cm^{-1}, as found in the silicate samples. The peak at 970 cm^{-1} of Ce-MCM-48 was attributed to Si–O–Ce and Si–O tensile vibrations [47]. The asymmetric tensile vibration peak intensity of the Ce(F)-MCM-48-0.10 molecular sieve increased at 1,088 cm^{-1}. This indicated that the chemical bond structure was altered after the introduction of F and the crystallinity was higher, which was consistent with the XRD results in Figure 1. For Ce(F)-MCM-48-0.10, there was a symmetrical tensile vibration at 810 cm^{-1}. These characteristic peaks narrowed and exhibited a red shift after the introduction of F [48]. For the Pd/Ce(F)-MCM-48-0.10 sample, the single peaks were again weakened, which may be related to the F–Si structures formed in the molecular sieve and the coordination bond formed between Pd and the support. Theoretically, Pd–O stretching vibration should be observed at 486 cm^{-1} in the Pd/Ce(F)-MCM-48-0.10 sample. However, as the infrared spectrum was not sensitive to the coordination bond and the palladium content was low, this vibration was not detected. Only weakened absorption peaks at 486 cm^{-1} were observed, which also verified the existence of the vibration.

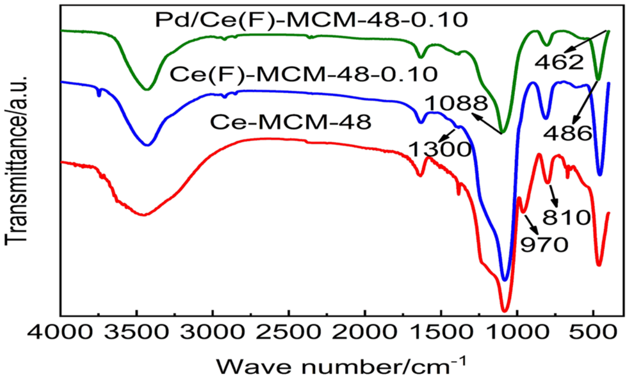

Figure 9: FT-IR spectra.

3.7 Catalytic performance evaluation

3.7.1 Effect of different Pd supports on the isomerization performance of *n*-heptane

Pd/MCM-48, Pd/Ce-MCM-48, and Pd/Ce(F)-MCM-48-0.10 were prepared with a Pd mass fraction of 0.4%. Figure 10 shows that *n*-heptane conversion was 8.8% and the selectivity was 11.2% for the Pd/MCM-48 catalyst. The catalytic performance was the lowest as the support was not acidic. After Ce was introduced into the support, the acidity increased, the isomerized carbocations were rapidly desorbed from the acid sites, which inhibited the cracking reaction. The *n*-heptane conversion was 47.5% and the selectivity was 76.2% for the Pd/Ce-MCM-48 catalyst. The oxidation state of the metal catalyst remained unchanged after the introduction of F, which was conducive to the transfer of electrons from the support to the metal oxide, subsequently promoting the catalytic reaction [49]. Its larger pore size and shape selectivity enabled the rapid diffusion of isoheptane in the catalyst and reduced the product retention time, which in turn prevented secondary reactions such as cracking and improved the hydroisomerization performance to a certain extent. The chemical environment on the support surface was beneficial in regulating the electronic and geometric properties of the dispersed Pd species. Furthermore, the support enabled the species to exhibit excellent chemical properties [36]. The *n*-heptane conversion was 67.3% and the isoheptane selectivity was 96.5% for the Pd/Ce(F)-MCM-48-0.10 catalyst, which demonstrated the improved isomerization properties. As shown in Table 3, the effect metal modified catalyst on the hydroisomerization properties of n-heptane reported in the literature.

3.7.2 Effect of reaction temperature on the catalytic performance of 0.4% Pd/Ce(F)-MCM-48-0.10

Figure 11 showed the catalytic performance curve of the 0.4% Pd/Ce(F)-MCM-48-0.10 catalyst for *n*-heptane isomerization at different reaction temperatures. With reaction

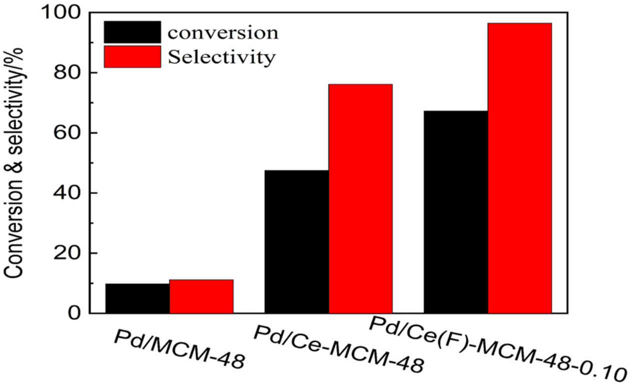

Figure 10: Catalytic performance of *n*-heptane isomerization of the catalyst with different supports.

Table 3: Effect of metal modified catalyst on the hydroisomerization properties of *n*-heptane

Catalyst	Reaction temperature (K)	Reduction temperature (K)	Conversion (%)	Selectivity (%)	Reference
0.4% Pd/Ce(F)-MCM-48-0.10	503	673	67.3	96.5	This paper
Pt/HBM	513	—	55.76	86.11	[27]
M-MCM-48 (M = Zr, Mg)	533/553	673	55.2/91.5	48/72.3	[50]
Mo-MCM-48	523	673	36.71	52.41	[12]
Pt/HBS	513	—	75.57	90.04	[2]
Pt-Beta	563	723	90.7	55.8	[28]
Pt/SBB-25	563	723	81.4	86.4	[28]
Pt/ASA	473–673	573	80.9	81	[3]
Mo/ASA	473–673	573	82	80	[3]
Mo/Al-SBA-15	473–673	573	83	69	[3]
0.5% Pt/5%MoO_3-HBEA	523	673	81.6	43.5	[4]
PtSn(2)-micro-SAPO11	523	673	<60	<60	[51]
PZH-0.3	533	723	81.1	94.2	[52]
1% Pt/SBA-15	673	723	85	–	[5]
0.05% Pt1@CeOx/SAPO-11	633	523	57.9	89.4	[53]

temperatures between 220 and 360°C, *n*-heptane conversion increased as the reaction temperature increased, while the isomerization selectivity exhibited a downward trend. The isomerization of *n*-heptane was a micro-exothermic reaction, but if the reaction temperature was too low, the overall reaction rate would be slow, resulting in an unsatisfactory conversion. Therefore, the reaction temperature needed to be increased. Only after reaching the specific reaction temperature, the reactants would be activated and the number of activated molecules increased. The increased number of effective reactant collisions was conducive to the reaction. When the reaction temperature was 280°C, the *n*-heptane conversion was 67.3% and the isomerization selectivity was 96.5%. At this time, the maximum isoheptane yield was 64.9%. Pyrolysis was endothermic, while *n*-heptane isomerization was exothermic. According to the thermodynamic equilibrium, it could be learned that continuously increasing the temperature will promote endothermic pyrolysis and may even cause excessive carbon deposits on the catalyst surface, resulting in decreased activity, a lower conversion of *n*-heptane, and a reduced yield. Excessive reaction temperatures could also cause the skeleton structure of the catalyst to collapse. When the reaction temperature exceeded 280°C, the yield gradually decreased. Therefore, the optimal reaction temperature was 280°C.

3.7.3 Effect of reaction duration on the catalytic performance of 0.4% Pd/Ce(F)-MCM-48-0.10

Figure 12 shows the catalytic performance curve of the 0.4% Pd/Ce(F)-MCM-48-0.10 catalyst for *n*-heptane isomerization at the reaction duration. When the reaction temperature was fixed at 280°C, the conversion of *n*-heptane and isomerization selectivity increased with the extension

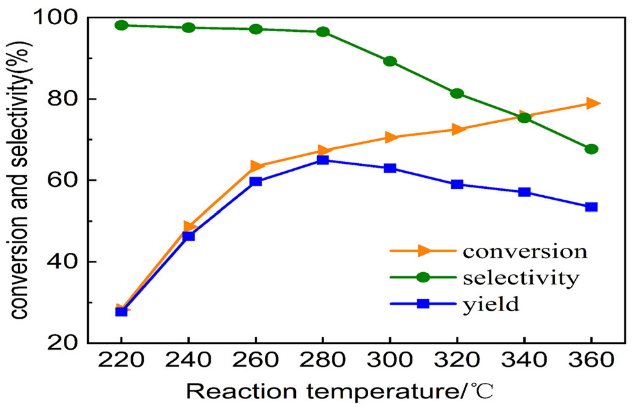

Figure 11: Catalyst performance of 0.4% Pd/Ce(F)-MCM-48-0.10 as a function of reaction temperature.

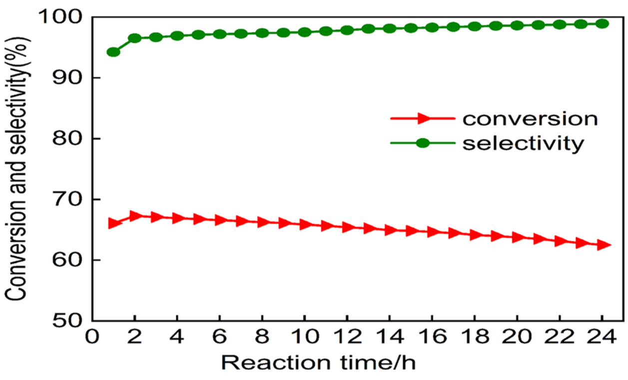

Figure 12: Catalyst performance of 0.4% Pd/Ce(F)-MCM-48-0.10 as a function of reaction time.

of reaction duration within 0–2 h. The conversion of *n*-heptane was 67.3% and the isomerization selectivity was 96.5% when the reaction duration exceeded 2 h. Compared with previous studies [6,12,26], excellent catalytic performance was achieved in a relatively short period, which was probably related to the excellent mass transfer rate of the catalyst. When the reaction duration was extended to 24 h, the catalytic performance slowly decreased, and the conversion of *n*-heptane dropped to 62.5%. This may be due to the formation of some carbon deposits on the active center of the catalyst which lowered the conversion rate as the reaction progressed. Furthermore, the collapse of the pore channels, blockage of the pore structure, loss of acid sites, etc., also caused the catalyst activity to decrease. During the 24 h continuous reaction, the selectivity increased slightly to 98.9%. This was probably due to carbon deposition at the strong acid center that catalyzed the pyrolysis [54], thereby improving isomerization selectivity. The reaction duration test of the catalyst showed that the catalyst exhibited satisfactory stability. For further understanding the as-prepared catalysts of the *n*-heptane hydrogenation conversion, the consideration of the reaction mechanism was vital. According to the literature [3,12,28,52], the reaction of long-chain alkanes on metal-support bifunctional catalysts was generally considered a bifunctional mechanism. While in this study, the precious metal Pd was loaded on the Ce(F)-MCM-48-0.10 mesoporous molecular sieve to prepare the catalyst, which could be inferred that the conventional bifunctional mechanism was followed. It was generally believed that the isomerization was completed through the bifunctional reaction mechanism on the above catalysts. The catalytic mechanism was usually loading precious metal Pd on acid supports. *N*-heptane dehydrogenated at the precious metal Pd active sites to form olefins, then the olefins migrated to the acid sites and underwent isomerization reactions, thereby generating isomer olefins, and finally the isomer olefins were hydrogenated at the precious metal active sites to generate the product, isoheptane. It provided hydrogenation/dehydrogenation function at metal sites, and protonation/deprotonation and skeleton rearrangement function at acid sites.

4 Conclusion

1. When the molar ratio of the reaction raw materials was *n*(Ce):*n*(TEOS) = 0.02 and *n*(NaF):*n*(TEOS) = 0.10, Ce and F were used as structural additives, the Ce(F)-MCM-48-0.10 molecular sieve was characterized by a high degree of order, increased specific surface area and pore volume, uniform pore size distribution, augmented acid content, and enhanced acidity. The specific order was Ce(F)-MCM-48-0.10 > Ce-MCM-48 > MCM-48.
2. Pd/Ce(F)-MCM-48-0.10 catalyst demonstrated a satisfactory degree of order and Pd dispersion a high effective loading percentage, and a slight loss of Ce and F after the impregnation of Pd. The prepared bifunctional catalyst had the metal sites and the acidic sites of the support. Under the synergistic effect of Ce and F, the Ce(F)-MCM-48-0.10 molecular sieve proved to be a good support for the dispersion of Pd nanoparticles.
3. Based on the study on the catalyst performance of the isomerization reaction of *n*-heptane, under the conditions of the optimal precious metal Pd loading of 0.4%, the reaction temperature of 280°C, and a reaction time of 24 h, the conversion of *n*-heptane isomerization was 67.3%, and the selectivity of isoheptane was 96.5%, and the catalytic performance of Pd/Ce(F)-MCM-48-0.10 was relatively stable. For the Pd-loaded catalyst with MCM-48 as the support for heptane isomerization, it was necessary to modify MCM-48 with Ce and F synergistically.

Acknowledgement: The authors acknowledge the support of Analysis and Test Center of Northeast Petroleum University.

Funding information: This work was supported by both the Support Plan for Outstanding Scientific Research Talents of Provincial Advantageous and Characteristic Disciplines of Chemical Engineering and Technology of Northeast Petroleum University and Natural Science Foundation of Heilongjiang Province, China (No. LH2021E012).

Author contributions: Yanhong Cui: writing – original draft, writing – review and editing, methodology, conceptualization, software, and investigation; Yanhua Suo: validation, visualization, and supervision; Wei Zhang: formal analysis, writing – review and editing; Yingjun Wang: project administration, funding acquisition, and resources; Chunhong Nie: project administration and formal analysis; Yanhong Wang: formal analysis and data analysis.

Conflict of interest: The authors state no conflict of interest.

Data availability statement: All data generated or analyzed during this study are included in this published article.

References

[1] Huang J, Wang J, Huang Z, Liu T, Li H. Photothermal technique-enabled ambient production of microalgae biodiesel: Mechanism

and life cycle assessment. Bioresource Technol. 2022;369:128390. doi: 10.1016/J.BIORTECH.2022.128390.

[2] Bahari MB, Jalil AA, Mamat CR, Hassan NS, Razak MH, Izzudin NM. Mechanistic studies of lower temperature isomerization of n-heptane over fibrous silica molybdenum catalyst. Int J Hydrogen Energ. 2022;252:653–65. doi: 10.1016/j.ijhydene.2023.03.321.

[3] Harmel J, Roberts T, Zhang Z, Sunley G, de Jongh P, de Jong KP. Bifunctional molybdenum oxide/acid catalysts for hydroisomerization of n-heptane. J Cat. 2020;390:161–9. doi: 10.1016/j.jcat.2020.08.004.

[4] Teh LP, Setiabudi HD, Sidik SM, Annuar NHR, Jalil AA. Synergic role of platinum (Pt) and molybdenum trioxide (MoO_3) promoted HBEA zeolite towards n-heptane isomerization. Mater Chem Phys. 2021;263:124406. doi: 10.1016/j.matchemphys.2021.124406.

[5] Ali NS, Alismaeel ZT, Majdi HS, Salih HG, Abdulrahman MA, Cata Saady NM, et al. Modification of SBA-15 mesoporous silica as an active heterogeneous catalyst for the hydroisomerization and hydrocracking of n-heptane. Heliyon. 2022;8(6):1–6. doi: 10.1016/J.HELIYON.2022.E09737.

[6] Harmel J, van der Wal LI, Zečević J, de Jongh PE, de Jong KP. Influence of intimacy for metal-mesoporous solid acids catalysts for n-alkanes hydro-conversion. Catal Sci Technol. 2020;10(7):2111–9. doi: 10.1039/c9cy02510c.

[7] Xie W, Wang H. Grafting copolymerization of dual acidic ionic liquid on core-shell structured magnetic silica: A magnetically recyclable Brönsted acid catalyst for biodiesel production by one-pot transformation of low-quality oils. Fuel. 2021;283:1–12. doi: 10.1016/j.fuel.2020.118893.

[8] Xie W, Han Y, Wang H. Magnetic Fe_3O_4/MCM-41 composite-supported sodium silicate as heterogeneous catalysts for biodiesel production. Renew Energ. 2018;125:675–81. doi: 10.1016/j.renene.2018.03.010.

[9] Xie W, Zang X. Immobilized lipase on core–shell structured Fe_3O_4-MCM-41 nanocomposites as a magnetically recyclable biocatalyst for interesterification of soybean oil and lard. Food Chem. 2016;194(C):1283–92.

[10] Li H, Fang Z, Smith R, Yang S. Efficient valorization of biomass to biofuels with bifunctional solid catalytic materials. Prog Energ Combust. 2016;55(jul):98–194. doi: 10.1016/j.pecs.2016.04.004.

[11] Boro A, Talukdar AK. Phenol hydroxylation over Fe and Co-loaded mesoporous MCM-48. J Porous Mater. 2019;26(4):1185–96. doi: 10.1007/s10934-018-0709-x.

[12] Ghaderi Z, Peyrovi MH, Parsafard N. Effects of Zr, Al, and mordenite on Pt-MCM-48 catalyst in n-heptane isomerization: preparation, characterization and catalytic performance. J Porous Mater. 2023;26(5):1279–86. doi: 10.1007/s10934-023-01463-x.

[13] dos Santos TG, Silva AOS, Pedrosa AMG, Araujo AS, Souza MJB. Structure and catalytic activity of highly ordered AlMCM-48 materials with different Si/Al ratios on the degradation of high-density polyethylene. J Porous Mater. 2021;28(3):919–28. doi: 10.1007/s10934-021-01044-w.

[14] Liu Y, Wang W, Xu X, Marcel Veder J-P, Shao Z. Recent advances in anion-doped metal oxides for catalytic applications. J Mater Chem A. 2019;7(13):7280–300. doi: 10.1039/c8ta09913h.

[15] Zhang M, Lin JH, Jin CM, Xiao JC. Difluorocarbene-based cyanodifluoromethylation of alkenes induced by a dual-functional Cu-catalyst. Chem Commun (Camb). 2021;57(21):2649–52. doi: 10.1039/d1cc00160d.

[16] Jiang J, Ding W, Li H. Promotional effect of F for Pd/HZSM-5 catalyst on selective HDO of biobased ketones. Renew Energ. 2021;179:1262–70. doi: 10.1016/j.renene.2021.07.065.

[17] Yang C, Tian Y, Pu J, Chi B. Anion fluorine-doped $La_{0.6}Sr_{0.4}Fe_{0.8}Ni_{0.2}O_{3-\delta}$ perovskite cathodes with enhanced electrocatalytic activity for solid oxide electrolysis cell direct CO_2 electrolysis. ACS Sustain Chem Eng. 2022;10(2):1047–58. doi: 10.1021/acssuschemeng.1c07576.

[18] Modak A, Mondal J, Aswal VK, Bhaumik A. A new periodic mesoporous organosilica containing diimine-phloroglucinol, Pd(II)-grafting and its excellent catalytic activity and trans-selectivity in C-C coupling reactions. J Mat Chem. 2010;20(37):8099–106. doi: 10.1039/C0JM01180K.

[19] Modak A, Bhaumik A. Surface-exposed Pd nanoparticles supported over nanoporous carbon hollow tubes as an efficient heterogeneous catalyst for the CC bond formation and hydrogenation reactions. J Mol Catal A-Chem. 2016;425:147–56. doi: 10.1016/j.molcata.2016.09.037.

[20] Roy S, Mondal DK, Chatterjee S, Chowdhury A, Khan TS, Haider MA, et al. Selective CO_2 reduction to methane catalyzed by mesoporous Ru-Fe_3O_4/CeOx-SiO_2 in a fixed bed flow reactor. Mol Catal. 2022;528:112486. doi: 10.1016/J.MCAT.2022.112486.

[21] Chen C, Chen F, Zhang L, Pan S, Bian C, Zheng X, et al. Importance of platinum particle size for complete oxidation of toluene over Pt/ZSM-5 catalysts. Chem Commun. 2015;51(27):5936. doi: 10.1039/c4cc09383f.

[22] Li Z, Dong X, Zhang M, Leng L, Chen W, Horton J, Hugh, et al. Selective hydrogenation on a highly active single-atom catalyst of palladium dispersed on ceria nanorods by defect engineering. Acs Appl Mater Inter. 2020;12(51):57569–77. doi: 10.1021/ACSAMI.0C17009.

[23] Schumacher K, Grün M, Unger KK. Novel synthesis of spherical MCM-48. Microporous Mesoporous Mater. 1999;27(2):201–6. doi: 10.1016/S1387-1811(98)00254-6.

[24] Wang L, Zhang J, Chen F, Anpo M. Fluoride-induced reduction of CTAB template amount for the formation of MCM-48 mesoporous molecular sieve. J Phys Chem C. 2007;111(37):13648–51. doi: 10.1021/jp0746805.

[25] Ma T, Xiong N, Tian Y, Zha G, Yang B, Xu B, et al. Analysis of KF behavior and inverse reaction molecular kinetics simulation in the vacuum carbothermic reduction of magnesium oxide. J Alloy Compd. 2023;955:1–15. doi: 10.1016/J.JALLCOM.2023.170325.

[26] Wang Y, Cui Y, Suo Y, Zhang W. Influences of cerium on structure and catalytic performance of n-heptane hydroisomerization of Ni-HPW/MCM-48. J Rare Earth. 2015;33(1):46–55. doi: 10.1016/s1002-0721(14)60382-3.

[27] Gao L, Shi Z, Etim UJ, Wu P, Han D, Xing W, et al. Beta-MCM-41 micro-mesoporous catalysts in the hydroisomerization of n-heptane: Definition of an indexed isomerization factor as a performance descriptor. Microporous Mesoporous Mater. 2019;277:17–28. doi: 10.1016/j.micromeso.2018.10.015

[28] Fedyna M, Śliwa M, Jaroszewska K, Trawczyński J. Effect of zeolite amount on the properties of Pt/(AlSBA-15 + Beta zeolite) micro-mesoporous catalysts for the hydroisomerization of n-heptane. Fuel. 2020;280:118607. doi: 10.1016/j.fuel.2020.118607.

[29] Mureseanu M, Filip M, Somacescu S, Baran A, Carja G, Parvulescu V. Ce, Ti modified MCM-48 mesoporous photocatalysts: Effect of the synthesis route on support and metal ion properties. Appl Surf Sci. 2018;444:235–42. doi: 10.1016/j.apsusc.2018.03.053.

[30] Benaissa M, Alhanash AM, Eissa M, Aldalbahi A, Alzahly S, Rahaman M, et al. The effect of mesoporous support on the catalytic performance of Pd nanoparticles in the hydrogenation of cyclopentene. J Porous Mater. 2020;27(6):1735–43. doi: 10.1007/s10934-020-00949-2.

[31] Zhan W, Guo Y, Wang Y, Liu X, Guo Y, Wang Y, et al. Synthesis of lanthanum-doped MCM-48 molecular sieves and its catalytic performance for the oxidation of styrene. J Phys Chem B. 2007;111(42):12103–10. doi: 10.1021/jp074521l.

[32] Rabinovich EM, Wood DL. Fluorine in silica gels. MRS Online Proc Libr. 1986;73(1):251–9. doi: 10.1557/PROC-73-251.

[33] Chang S, Jia Y, Zeng Y, Qian F, Guo L, Wu S, et al. Effect of interaction between different CeO_2 plane and platinum nanoparticles on catalytic activity of Pt/CeO_a in toluene oxidation. J Rare Earth. 2022;40(11):1743–50. doi: 10.1016/j.jre.2021.10.009.

[34] Kaneda M, Tsubakiyama T, Carlsson A, Sakamoto Y, Ohsuna T, Terasaki O, et al. Structural study of mesoporous MCM-48 and carbon networks synthesized in the spaces of MCM-48 by electron crystallography. J Phys Chem B. 2002;106(6):1256–66. doi: 10.1021/jp0131875.

[35] Pu X, Yao L, Yang L, Jiang W, Jiang X. Utilization of industrial waste lithium-silicon-powder for the fabrication of novel nap zeolite for aqueous Cu(II) removal. J Clean Prod. 2020;265:121822. doi: 10.1016/j.jclepro.2020.121822.

[36] Dong C, Zhou Y, Ta N, Liu W, Li M, Shen W. Shape impact of nanostructured ceria on the dispersion of Pd species. Chinese J Catal. 2021;42(12):2234–41. doi: 10.1016/s1872-2067(20)63725-1.

[37] Ma Y, Xu Y, Chen H, Guo J, Wei X, Huang L. Supported on mesoporous silica nanospheres, molecularly imprinted polymer for selective adsorption of dichlorophen. Green Proces Synth. 2021;10(1):336–48. doi: 10.1515/gps-2021-0030.

[38] Ning C, Xu M, Hui DC-W, Lin CSK, McKay G. Study of quench effect on heavy metal uptake efficiency by an aluminosilicate-based material. Chem Eng J. 2017;311:37–45. doi: 10.1016/j.cej.2016.11.078.

[39] Liu Z, Guan D, Yu Q, Xu L, Zhuang Z, Zhu T, et al. Monodisperse and homogeneous SiO/C microspheres: A promising high-capacity and durable anode material for lithium-ion batteries. Energy Stor Mater. 2018;13:112–8. doi: 10.1016/j.ensm.2018.01.004.

[40] Bedoya JC, Valdez R, Cota L, Alvarez-Amparán MA, Olivas A. Performance of Al-MCM-41 nanospheres as catalysts for dimethyl ether production. Catal Today. 2022;388–389:55–62. doi: 10.1016/j.cattod.2021.01.010.

[41] Guo C, Wang D, Liu T, Zhu J, Lang X. A three dimensional SiOx/C@RGO nanocomposite as a high energy anode material for lithium-ion batteries. J Mater Chem A. 2014;2(10):3521–7. doi: 10.1039/C3TA13746E.

[42] Xu Q, Chu M, Liu M, Zhang J, Jiang H, Li C. Fluorine-triggered surface reconstruction of Ni_3S_2 electrocatalysts towards enhanced water oxidation. Chem Eng J. 2021;411:128488. doi: 10.1016/j.cej.2021.128488.

[43] Akula S, Balasubramaniam B, Varathan P, Sahu AK. Nitrogen–fluorine dual doped porous carbon derived from silk cotton as efficient oxygen reduction catalyst for polymer electrolyte fuel cells. ACS Appl Energy Mater. 2019;2(5):3253–63. doi: 10.1021/acsaem.9b00100.

[44] Wang Z, Huang Z, Brosnahan JT, Zhang S, Guo Y, Guo Y, et al. Ru/CeO_2 catalyst with optimized CeO_2 support morphology and surface facets for propane combustion. Environ Sci Technol. 2019;53(9):5349–58. doi: 10.1021/acs.est.9b01929.

[45] Li S, Li X, Wu H, Sun X, Gu F, Zhang L, et al. Mechanism of synergistic effect on electron transfer over Co-Ce/MCM-48 during ozonation of pharmaceuticals in water. ACS Appl Mater Interfaces. 2019;11(27):23957–71. doi: 10.1021/acsami.9b02143

[46] Shang Q, Tang N, Qi H, Chen S, Xu G, Wu C, et al. A palladium single-atom catalyst toward efficient activation of molecular oxygen for cinnamyl alcohol oxidation. Chinese J Catal. 2020;41(12):1812–7. doi: 10.1016/S1872-2067(20)63651-8.

[47] Shao Y, Wang L, Zhang J, Anpo M. Synthesis of hydrothermally stable and long-range ordered Ce-MCM-48 and Fe-MCM-48 materials. J Phys Chem B. 2005;109(44):20835–41. doi: 10.1021/jp054024.

[48] Zhang Y, Kang W, Han H, Wang H, Chen Y, Gong X, et al. In-situ synthesis of NaP zeolite doped with transition metals using fly ash. J Am Ceram Soc. 2019;102(12):7665–77. doi: 10.1111/jace.16623.

[49] Zhang R, Wang Y, Yu ZQ, Sun ZC, Wang AJ, Liu YY. Molybdenum peroxide anchored on fluoronated UiO-66 as Catalyst in the oxidation of sulfur containing comp. Chem J Chineses Univ Chinese. 2021;42(6):1914–23 (in Chinese). doi: 10.7503/cjcu20200789.

[50] Wang Y, Dong X, Ma S, Wang J, Li X, Suo Y, et al. Study on Synthesis of Mesoporous M-MCM-48(M = Zr,Mg) and Its Activity for Isomerization of n-Heptane. China Pet Process Pe. 2018;20(03):62–72.

[51] Said S, Zaky Magdy T. PtSn supported on hierarchical mesoporous SAPO-11: Synthesis, characterization and catalytic evaluation in n-heptane hydroisomerization. J Organomet Chem. 2022;957. doi: 10.1016/J.JORGANCHEM.2021.122180.

[52] Guo K, Ma A, Wang Z, Li J, Wu B, Liu T, et al. Investigation of n-heptane hydroisomerization over alkali-acid-treated hierarchical Pt/ZSM-22 zeolites. New J Chem. 2022;46:16752. doi: 10.1039/d2nj02820d.

[53] Qin H, Feng N, Lv Q, Wan H, Guan G. Pt single atom-anchored CeOx/SAPO-11 for highly efficient hydroisomerization of n-heptane. Fuel Process Technol. 2023;241:1–9. doi: 10.1016/J.FUPROC.2022.107604.

[54] Houzvicka J, Hansildaar S, Nienhuis JG, Ponec V. The role of deposits in butene isomerisation. Appl Catal A-Gen. 1999;176(1):83–9. doi: 10.1016/S0926-860X(98)00235-X.